

The In-Flight Performance of the SOHO/CDS Grazing Incidence Spectrometer [with added tables]

N.P.M. Kuin, G. Del Zanna

*University College London, Mullard Space Science Laboratory, Holmbury St. Mary,
Dorking, Surrey RH5 6NT, UK*

October 12, 2007

Abstract. We present the characteristics, operations history, performance and calibration of the GIS spectrograph of the Coronal Diagnostic Spectrometer on-board SOHO. The GIS sensitivity has been monitored in a direct manner by examining the quiet sun count rates during 1996-2006, nearly a whole solar cycle of observations. Overall, the instrument, with its grazing-incidence optics and Microchannel Plates (MCP), has performed exceptionally well. For most spectral regions, changes in the instrument sensitivity have been very small over a ten-year period. The trends in sensitivities support the use of the radiometric calibration of Del Zanna et al. (2001, *Astron. Astrophys.* **379**, 708) throughout the mission. The verification of the detector performance over such a long period allows us to point out the spectral lines that can reliably be used for scientific analysis.

Four tables have been added in Appendix 3 with the initial determinations of the sensitivity changes which can be used to calibrate the data. These tables were not part of the published work and should be considered preliminary.

1. Introduction

The Coronal Diagnostic Spectrometer (CDS) on board the Solar and Heliospheric Observatory (SOHO) has been described by Harrison et al. (1995). Two systems, the Normal Incidence Spectrometer (NIS), and the Grazing Incidence Spectrometer (GIS), share the front optics, scan mirror and slits. The NIS provides complementary capabilities to GIS spectrally as well as spatially. Indeed, the two instruments were originally designed to complement each other by covering almost entirely a wide spectral range, from 150 to 790 Å.

Over the last ten years of operations, a large and valuable dataset of GIS observations has been obtained. GIS has recorded a wealth of EUV spectral lines of, e.g., C III–IV, N III–IV, O II–VI, Ne V–VII, Mg VI–IX, Si IV–IX, Fe VIII–XXIV, which originate in the transition region and corona, covering temperatures ranging in $\log T$ [K] from 5.0 to 7.1. Obviously, for most scientific uses, an accurate radiometric calibration and understanding of the instrument must be achieved. For future instrumentation development it is also interesting to study the 10-year long behaviour of the detectors and optics in space. Aside from occasional sounding rocket flights, and the recently launched EIS instrument on Hinode, GIS is the only spectrometer

© 2007 Springer Science + Business Media. Printed in the USA.

that has simultaneously observed the solar corona in the spectral ranges observed by the broad-band imaging instruments such as the SOHO Extreme Ultraviolet Imaging Telescope (EIT), and the Transition Region and Corona Experiment (TRACE), and is therefore the only instrument that can provide direct continuous calibration for these instruments. It also provides essential spectral information to calibrate the Solar Extreme Ultraviolet Monitor (SEM), the EUV irradiance monitor on-board SOHO. GIS is also the only instrument that has observed the solar corona in its strongest coronal lines over a time-span of a solar cycle. These measurements are used to study long-term trends in the solar corona, in particular of the EUV spectral irradiance (Del Zanna, Andretta, and Beaussier, 2005).

The pre-launch GIS radiometric calibration was described in Bromage et al. (1996) and Lang et al. (2000), while some of the idiosyncrasies of the earlier GIS spectra were described in Landi et al. (1999). The first and only in-flight radiometric calibration of all first- and second-order channels of CDS was obtained by Del Zanna et al. (2001) with the use of specially-designed observations performed in the first few years of the SOHO mission (mostly in 1997). The calibration relied on the use of atomic data, and data from a 1997 rocket flight (Brekke et al., 2000) for the absolute calibration. Also, it was assumed that by 1997 any sensitivity losses in the stronger lines were negligible. An in-flight radiometric calibration in the EUV is notoriously difficult to achieve, and during the SOHO mission many efforts have been made to monitor the instrument's performance. Here, we provide the first report on the GIS performance and calibration. The detector characteristics and the operation history are briefly described as a necessary introduction to the instrument calibration. We also briefly describe the various attempts that have been made over the years to characterise the instrument's performance, and present a new simple method which makes use of ten years of regular quiet sun observations to study any sensitivity changes. Typical changes seen are related to the detector properties. A discussion of the methodology used for this examination of detector sensitivity is given.

2. The GIS detectors

The GIS grating provides astigmatic imaging of the slit on four detectors placed on a Rowland circle; the slit image is 16 mm long on the detector face. The four detectors cover the spectral ranges 151–222 Å (detector 1), 260–340 Å (det.2), 393–492 Å (det.3), and 656–784 Å (det.4), and also include second order lines in detectors 3 and 4. Observations can use any of the six slits of the CDS, but are usually confined to slit 1 (2"×2") or slit 2 (4"×4"). The GIS provides full spectral coverage in its spectral windows, and

can build up an image by rastering, using slit and scan mirror positioning, or alternatively by using the instrument pointing system (Harrison et al., 1995). Typical exposure times are 50s for slit 1 and 15s for slit 2 on the quiet regions in the studies used here.

Each detector consists of an uncoated z-stack multichannel plate (MCP), spiral anode (SPAN), readout electronics, and shared on-board science data processing that uses a lookup table for each detector. Some of the details can be found in Breeveld (1996), and Breeveld and Thomas (1992).

The SPAN consists of three co-planar, electrically isolated electrodes, *A*, *B*, and *C*, spaced 3 mm behind the MCP. The pattern of the electrodes has a repetitive structure covering the entire active area. The pattern is finely divided such that the charge cloud associated with each photon detection ('event') is registered on all electrodes. The event location on the electrodes is determined from the relative areas of *A*, *B*, and *C* which vary uniquely along the electrode. The detector is thus sensitive to the event location in only one dimension, consistent with the astigmatic imaging of the slit in the other direction.

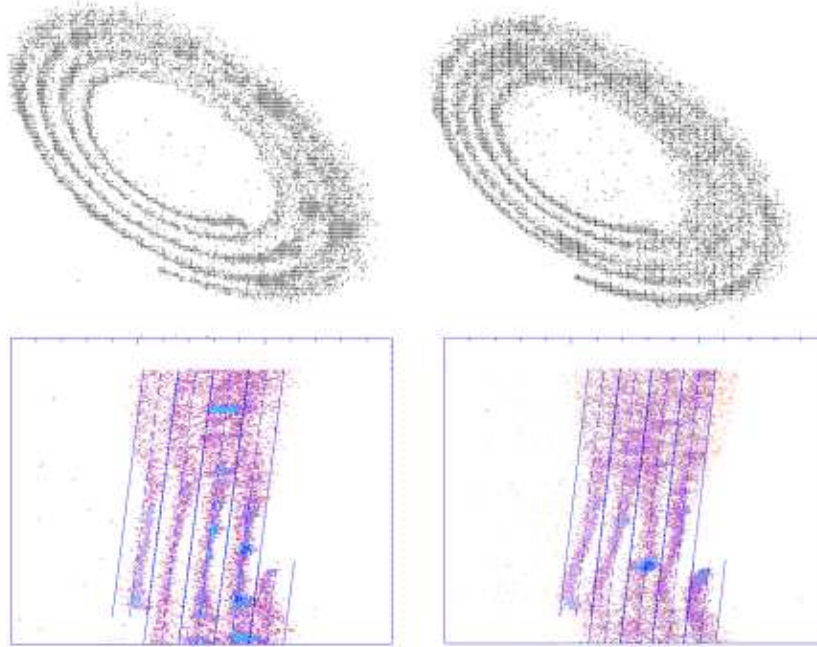
The charges coming off the *A*, *B*, and *C* electrodes are preamplified. Two of these electrode signals are digitized by radiometric analogue-to-digital converters after normalisation with the sum of all three signals. This gives two 8-bit values for each event. Therefore, each event can be mapped to a plane. An exposure leads to thousands of events arranged in the form of a spiral. The location of the spiral follows from the SPAN design and amplifier gains. Further details are provided in the Appendix. The sum signal is digitized separately to build a pulse height distribution (PHD). The PHD is used to reject counts outside of an acceptable range.

The detectors are nearly identical since they were built to be interchangeable. They have a low "dark" count rate of 2 s^{-1} per detector. With use, the quantum efficiency of the MCPs decreases at the locations of high illumination by spectral lines. This effect, called long-term gain depression (LTGD), can partially be counteracted by changing the voltage over the whole detector. Therefore, the detector sensitivity is expected to change over time due to LTGD as well as periodic updates to the high voltage (HV) over the MCP. Ageing of the electronics can affect the signal of each of the electrodes, as well as the sum reference, and thus has the potential to affect the measured count position.

Due to dead-time constraints, there is an unspecified loss of sensitivity for count rates larger than $50\,000 \text{ s}^{-1}$. This limit has hardly ever been reached. The typical count rates observed in slit 2 vary from 300 s^{-1} in the quiet sun, to 2000 s^{-1} in active regions.

The count-rate-dependent gain depression due to analogue dead time is a minor correction that has been characterised and is taken into account in the analysis software.

a) Feb. - Mar. 1996



b) Apr. - May 2006

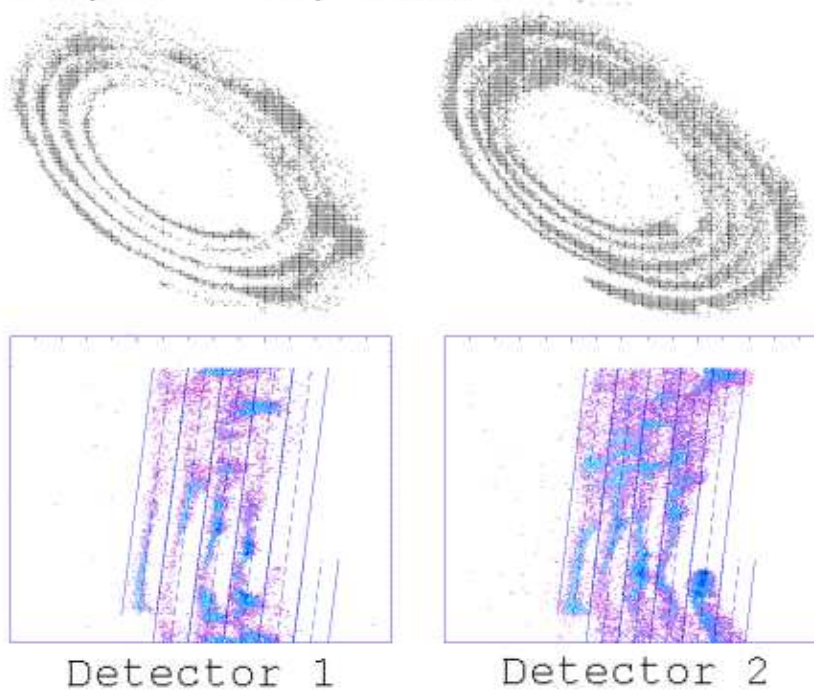


Figure 1. GIS raw data dumps for quiet sun regions, taken in 1996 (panel a) and 2006 (panel b) for detector 1 (left) and 2 (right). The upper plots in each panel show the data in the X-Y coordinates, in the shape of spirals. The lower plots in each panel show the gset fit in polar $r-\theta$ coordinates. These data and gset constitute the best fits at the time. The middle of the spiral swath is a dashed line, and the limits of the spiral path are drawn with continuous lines.

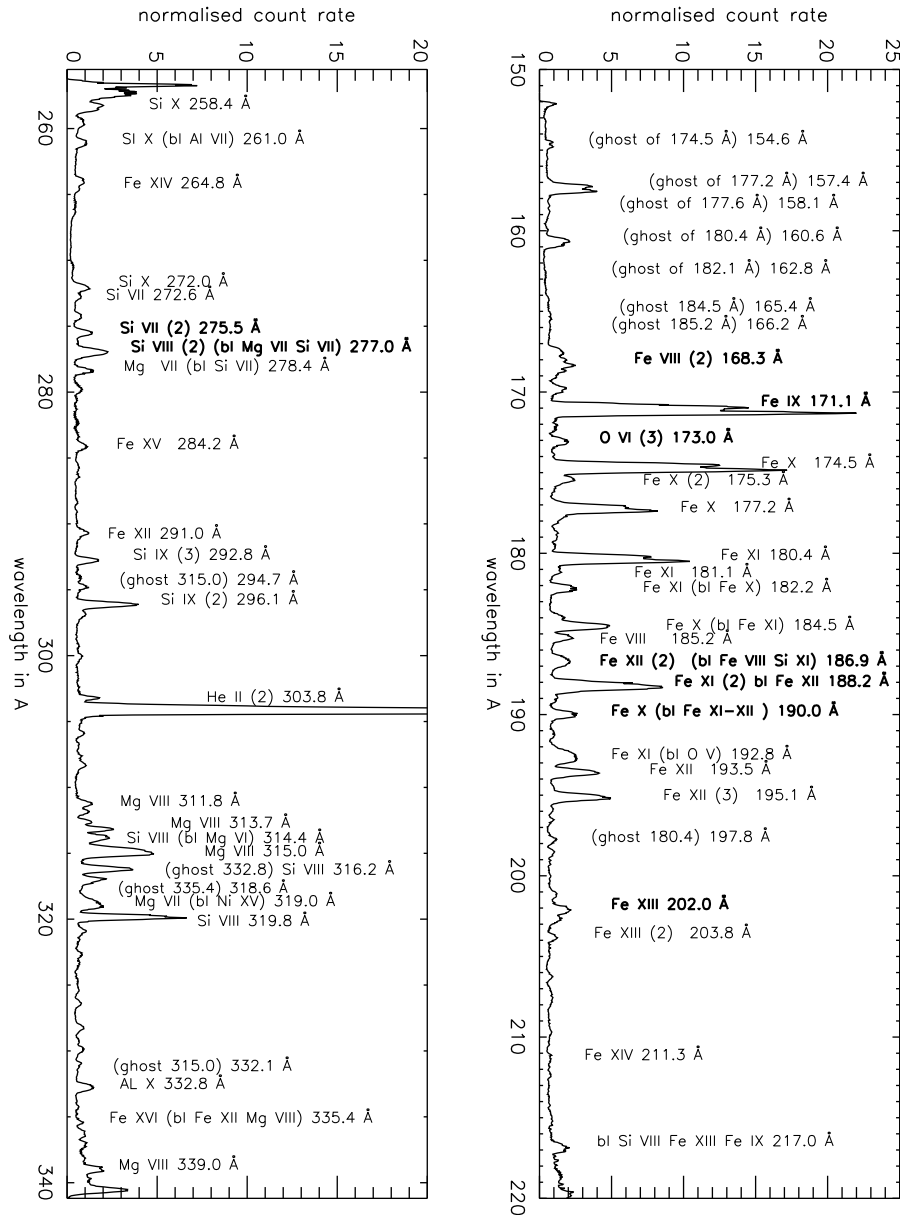


Figure 2. GIS annotated spectra for detectors 1 (left) and 2 (right) for quiet sun regions. Data were taken in early 1997, with identifications of prominent features based on CHIANTI. Notation is: *bl* for blends with other ions, *Ho* for second order lines, and *(n)* means self-blends with *n* lines. Lines without any ghost signature in the count rate histories are in bold type.

A further limitation arises from the digitisation to only 8-bits of the coordinate of each count. The counts fall in a spiral pattern in data space (see Figure 1), and recording their location with the normal (X,Y) digitisation means that, as measured along the spiral, at certain points the spectrum is under-sampled, and the counts appear in neighbouring pixels. In the spectrum this has the effect of creating a fixed noise pattern. However, this fixed pattern of noise does not affect the overall sensitivity as each spectral line is well resolved.

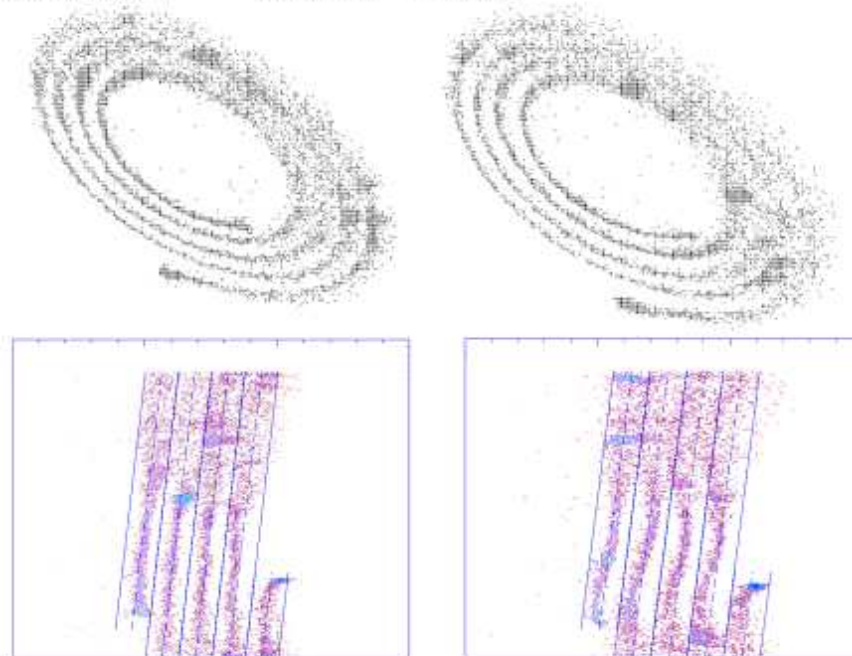
During normal operations the data of each event are binned on a 256×256 grid on board using a Look Up Table (LUT). The LUT is dynamically generated on board using a parameter set. Each parameter set is called 'gset'. Over the years, different gsets for each combination of detector, region type observed, and slit used have been created. Each gset contains the high voltage (HV) settings, as well as the LUT parameters. The HV settings mainly change due to MCP gain loss, while the other LUT parameter changes are mainly due to ageing electronics.

In a special operations mode which requires continuous contact, the (X,Y) coordinates of a random selection of events, as well as a sampling of the PHD on a single detector, have been obtained in order to generate the gsets. These are called 'raw data dumps', and are discussed below.

Two tungsten filaments are positioned on the side of the optics bench cavity in front of the detectors. When they are activated with a small current, they provide a source of electrons that impact the open MCP face. The original idea was to provide flat field exposures that could be used to monitor sensitivity changes. Behind each anode two thin wires, called stims, provide a check on the operation of the anode and electronics in the absence of a voltage over the MCPs.

Figures 1 and 3 shows the raw data dumps obtained in 1996 and 2006 from each of the detectors for a quiet Sun region. For each detector the number of raw counts used is the same in both data dumps. The raw data dumps are displayed in two ways: as a spiral in X and Y data coordinates (where the wavelength coordinate runs along the spiral), and in polar (r, θ) coordinates which are obtained after applying the gset parameters of the time. The stronger spectral lines can easily be identified on the spirals, and some clearly extend, in the cross-dispersion direction, over more than one spiral arm. Since the data are normally pre-processed on board via the LUT and mapped to a spiral, spectral lines that extend too far lose counts into the neighbouring spiral arms. In the spectra (Figures 2 and 4), these misplaced counts show up shifted by a well-known amount in wavelength. This is known as 'ghosting'. Stronger lines can ghost into both spiral arms, creating two ghosts. In some cases, where ghosts fall in regions free of spectral lines, 'de-ghosting' can be obtained during the analysis process. A problem arises when the ghosting overlaps with another spectral line.

a) Feb. - Mar. 1996



b) Apr. - May 2006

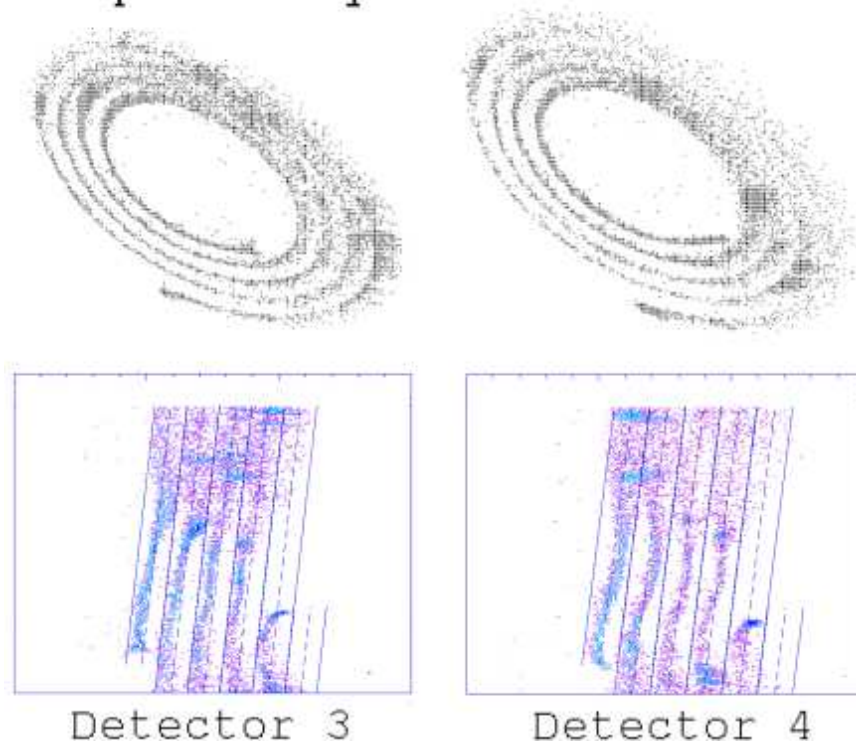


Figure 3. GIS raw data dumps for quiet sun regions, taken in 1996 (panel a) and 2006 (panel b) for detector 3 (left) and 4 (right). The upper plots in each panel show the data in the X-Y coordinates, in the shape of spirals. The lower plots in each panel show the gset fit in polar r - θ coordinates. These data and gset constitute the best fits at the time. The middle of the spiral swath is a dashed line, and the limits of the spiral path are drawn with continuous lines.

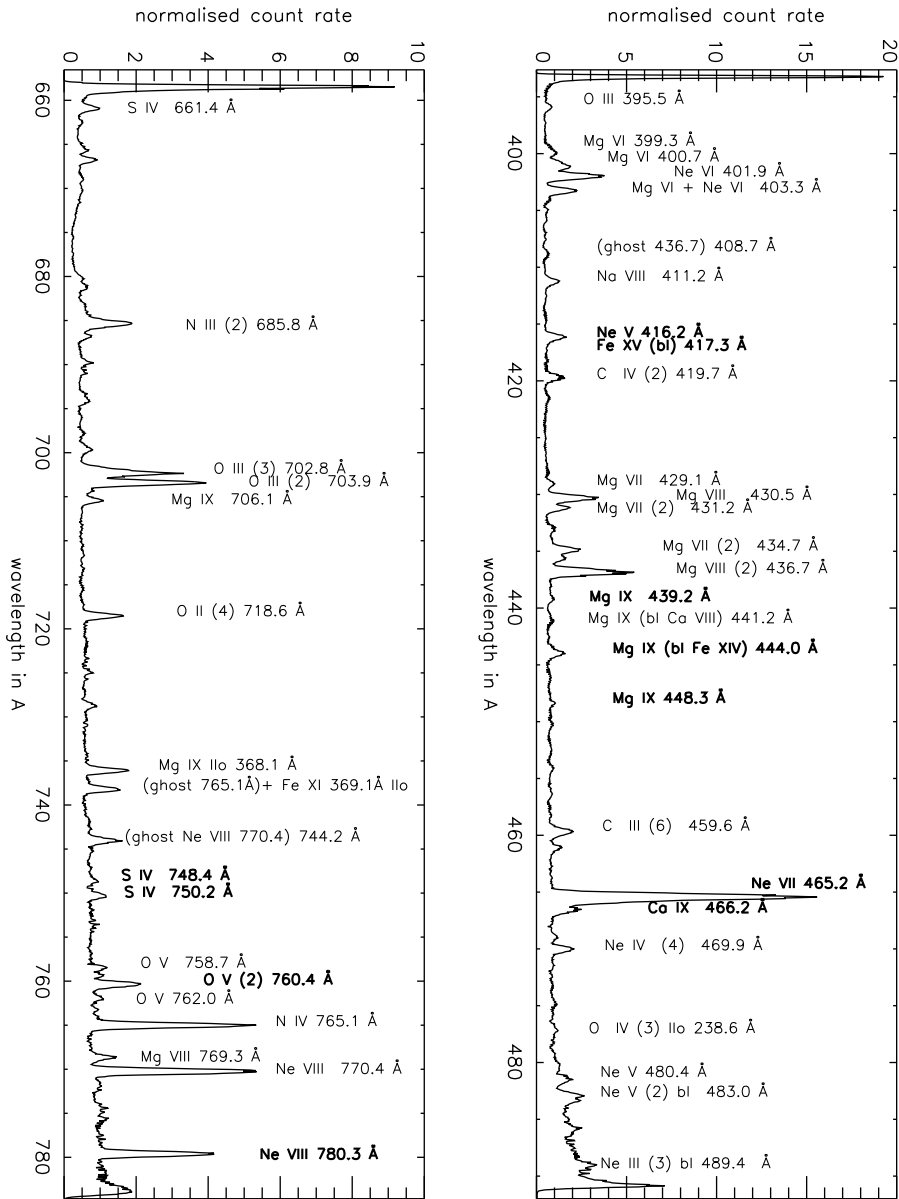


Figure 4. GIS annotated spectra for detectors 3 (left) and 4 (right) for quiet sun regions. Data were taken in early 1997; identifications have been provided for the most prominent line features.

Table 1. GIS Operations History

Launch-March 1996	Raw data dumps and filament dumps were obtained for all detectors and all permutations of slit, region, and HV setting. several gsets were used.
March 1996	gset 22 for the quiet sun becomes default.
June 1996	gset 41 replaced 22; similar gset updates for the other regions.
1997	Filament dumps obtained to monitor LTGD.
July 1998	SOHO attitude loss and recovery. A clear change is noticeable in some of the spectra after the event.
July 1998	The GIS pointing relative to the NIS changed (Kuin and Del Zanna, 2006), but this is not expected to affect the illumination of the detectors.
October 1999	Filament and raw data dumps. New gsets were generated (gset 65, 66, etc.).
2001	Raw data and filament dumps were obtained, but no changes to the major gsets were made. A few special gsets were updated, like the off-limb gset.
May 1999-June 2001	Detector 2 was switched off.
Mid-2001	A slit anomaly caused disabling of the movement of the slit in the N-S direction, hence rastering for GIS. The anomaly was not mechanical, and around November 2002 the instrument resumed normal operations.
2003	Filament dumps, raw data dumps.
July 2003	The spacecraft started periods of 180 degree roll due to problems with the main antenna.
2005	Detector 1 data became unreliable due to a need for new gsets.
March - May 2006	Filament and raw data dumps, new gsets (numbers 82 and 83, etc.).

The same spectral features always fall on the same place on the spiral because the photons always fall on the same place on the MCP face. Since spiral widths are sufficiently narrow on the lower-left side of the pattern, each detector has four spectral regions where no ghosting is present. An exception is the two outer spirals of detector 2, which lie so close that ghosting can occur if the gset is not fine-tuned.

Figure 1 shows that in detector 1 some spectral lines have grown outward over time, overlapping the next spiral. This increased width of the lines is the main reason why ghosting has increased over time. The increased ghosting is stronger for the lines with high count rates. (this detector records the strongest EUV coronal lines). Detector 2 changed greatly in the strong lines, particularly in He II 304 Å line. The spiral arms also become more

irregular. It can be seen that several spectral lines may ghost into other arms. Detectors 3 and 4 (see Figure 3) show little change in the spiral pattern, LTDG and ghosting. This is mainly due to the low incident count rates in these detectors. We have also examined the raw data for active regions, which have count rates nearly ten times higher. We found larger spiral patterns, and the need to set up separate gsets for active regions.

3. Operations History

The operations history has been summarized in Table 1.

During the SOHO loss of attitude control in 1998, the CDS instrument side was facing the Sun long enough for it to heat up to over 100° C. This probably did not affect the MCPs. However, the electronics were most likely affected by the high temperatures, changing the gain on the signals and thereby no longer matching the LUT being used. With the 1999 gset updates, all lines were restored to expected count rates, suggesting that no serious damage occurred due to the SOHO attitude loss.

The decision to switch off detector 2 for a certain period was made because the number of rejected PHD events was found to exceed the normal limits for operation. It is possible that contamination of the front face of the MCP in detector 2 was the cause. When switched on again, the detector appeared to have recovered, and has been used thereafter.

Due to the introduction of a periodic 180° change in the spacecraft roll angle after July 2003, north and south may not be the default direction in GIS rasters, since the arrays are filled with reference to the spacecraft coordinates. Care must be taken when positioning GIS data.

4. Calibration history

4.1. POINTING AND WAVELENGTH CALIBRATION

The pointing of the CDS has an accuracy of $10''$ and a $2''$ stability over a 30-minute period (Harrison et al., 1995). The pointing of the NIS has been maintained stable and in alignment with the instrument pointing, but since the SOHO attitude loss in 1998 the GIS has a $20.2''$ offset south, at zero roll angle (Kuin and Del Zanna, 2006).

A pre-launch calibration study (Bromage et al., 1996) showed that the GIS wavelengths are quadratic functions of pixel number, which depend on the LUT. Two wavelength calibrations are available: one based on gset 22 for LUT with 4.2 arms, and one based on gset 82 for LUT with 5.2 arms.

4.2. RADIOMETRIC CALIBRATION

The pre-launch GIS radiometric calibration was described by Breeveld (1996) and Lang et al. (2000). A secondary calibrated source of EUV radiation was used for those measurements. The combined systematic and random uncertainty of those measurements was estimated to be 30%. However, the in-flight calibration was found to be very different (factors of about 2). A complex set of observations and methods, which also relied on CHIANTI ¹ atomic data was then developed by Del Zanna (1999) and Del Zanna et al. (2001) to provide an internal calibration of all nine CDS channels, i.e., both NIS and GIS first and second order. The data were taken during several campaigns, mostly in 1997.

After two workshops held at the International Space Science Institute (ISSE) in Bern, Switzerland, the various teams converged to a consistent relative radiometric calibration between the various SOHO instruments within 30-50%, but only for the first years of the mission, and at few selected wavelengths (see the book ‘The radiometric calibration of SOHO’, Pauluhn, Huber and von Steiger (2002)).

The Del Zanna et al. (2001) radiometric calibration did not take into account possible LTGD effects in the GIS and NIS, which led Lang et al. (2002) to doubt its accuracy. A comparison with a low-resolution EUV Grating Spectrograph spectrogram, flown on a NASA/LASP rocket flight in 1997, indicated a drop in sensitivity in the stronger (NIS) He I 584 Å line by only 25% (Brekke et al., 2000), and minor corrections to most lines. This LTGD in the NIS has subsequently increased significantly, and work is still in progress to characterise it (Del Zanna and Andretta, 2006; Thompson, 2006).

For the GIS, there are no direct ways to measure the LTGD, and most of the effort we have devoted in the last few years was to find appropriate ways to characterise it. The 10-year-long data we have analysed show that during that time the counts fall on the mean long-term trends for most lines even though between 1997 and mid-1998 we see an anomalous drift in sensitivity in many lines.

Initially, filament exposures were used to determine the sensitivity loss over the face of the detector. However, the filaments illuminate the whole detector, while the image of the slit only covers the detector partially. Although the detector is extended in two dimensions, the readout is one-dimensional. Hence the correction for LTGD from the flat fields needs an assumption about which fraction of the detector in the direction normal to the dispersion has been affected by the gain depression. Other problems are related to the different PHD caused by the electrons and their differing incident angle, compared to the solar photons. LTGD is clearly visible in

¹ CHIANTI can be found at <http://www.CHIANTI.rl.ac.uk> (see Dere et al. (1997))

Table 2. Selected observations of the quiet sun

CDS program	slit (arcsec)	exposure time(sec)	raster (arcmin)	minutes per raster	gset ID's
SPECT_1	2×2	50	15x15	192	22, 40, 41, 65
G2AL	4×4	100	20x1	34	66
GISAT	4×4	15	10x20	56	66,75

the filament exposures, but shows very small changes in the 1996-1999 period. Confidence in the accuracy of the flat fielding process for sensitivity corrections was lost over time, and the correction for LTGD based on the flat fields was abandoned in 2003 in favour of a new method.

The new approach involved the determination of the sensitivity loss due to LTGD taking advantage of the fact that the detector voltage can be varied in flight. A special observational sequence (GIMCPS) was used to observe the quiet sun and determine the variations in the PHD as a function of voltage. The optimum response of the detector in certain spectral lines can be determined in this way (Lapington, 2004). The gain loss in selected lines was then determined as a function of the total number of counts measured over the life of the mission. Preliminary LTGD corrections based on the assumption that the gain loss in a MCP channel is proportional to the total charge extracted (as found by Malina and Coburn (1984)) were implemented in 2003 and are still used for the current GIS calibration. However, this method could not be fully exploited after 2004, because the GIMCPS sequence did not anticipate the large MCP gain loss in detector 1. Furthermore, this approach produced an overcorrection of a factor of two in the lines of detector 1. We have therefore chosen to use the 10 years of synoptic observations as a baseline to assess the LTGD.

5. Ten years of GIS data

Synoptic GIS observations of the quiet Sun have been routinely performed since 1996 up to the present (May 2007). The bulk of the dataset consists of $30'' \times 30''$ raster scans (SPECT_1), performed routinely with the exception of the period of the temporary loss of contact with SOHO (in 1998), and in 2002, when the GIS rastering was discontinued. A preliminary analysis of this dataset, up to 2003, was published by Del Zanna, Andretta, and Beaussier (2005). Here, we have extended this analysis to include other datasets. We used the observing programs listed in Table 2.

No corrections were applied to the data, the idea being that LTGD effects should clearly be evident as reductions in radiances in the stronger lines. The weaker lines, on the other hand, are expected to be less affected. Actually the only corrections of any significance that GIS data need are those for ghosting and for LTGD. In this respect, GIS spectra are very simple.

Given the high variability in the solar radiance, and the small field of view (FOV) of the GIS observations, we had to first select a good dataset of truly ‘quiet sun’ observations. A few hundred GIS observations spanning the 10 years have been visually inspected, and the FOV checked against near-simultaneous EIT observations, to select a good dataset. Spectra containing brightenings and high-temperature plasmas were rejected. This was based on the intensity in the λ Fe XVI 335.4 Å, Fe XV 417.3 Å, Fe XV 284.2 Å, and Fe XIV 211.3 Å coronal spectral lines. The strong spatial and temporal variability in the transition region lines was found to be largely removed by simply averaging over the FOV. Indeed the average radiances of the ‘quiet Sun’ transition region (TR) lines turn out to be remarkably stable over time. Obviously, no a-priori assumptions on the long-term trends in the radiances of the quiet Sun can be made. However, there are good reasons to expect that, at least in the lower-temperature lines of the chromosphere and TR, the radiances should be approximately constant. Ultimately, this is due to the small variations in the ‘salt and pepper’ magnetic fields in quiet areas (Pauluhn and Solanki, 2003). The radiances of the hotter lines are expected to increase during solar maximum, due to the fact that the entire solar corona becomes hotter. In any case, having observations that span an entire solar cycle greatly helps, since radiances should return to their quiescent state, unless of course cycle-to-cycle variations are present.

In 2001–2002 there were no SPECT_1 observations made and G2AL observations were used instead, which turn out to have a larger uncertainty because of a smaller number of counts; see table 2. The uncertainties in each line were calculated assuming Poisson statistics. The counts were averaged over all the pixels in each raster and normalised by exposure time and pixel area. The GISAT CDS program observations were used after 2003, replacing the SPECT_1 observations.

We used the IDL SolarSoft CFIT line fitting programs to fit gaussian profiles to line blends. The background was based on short line-free regions in the spectra, and is generally negligible. Exceptions are the end regions of each detector, which show some extra background due to spillage of electrons around the edge of the detector; and solar continuum in detectors 3 and 4.

5.1. GHOSTING

The total count rate history in some GIS spectral lines shows evidence of changes in ghosting. In the period 1996–1998 many lines show a drift in

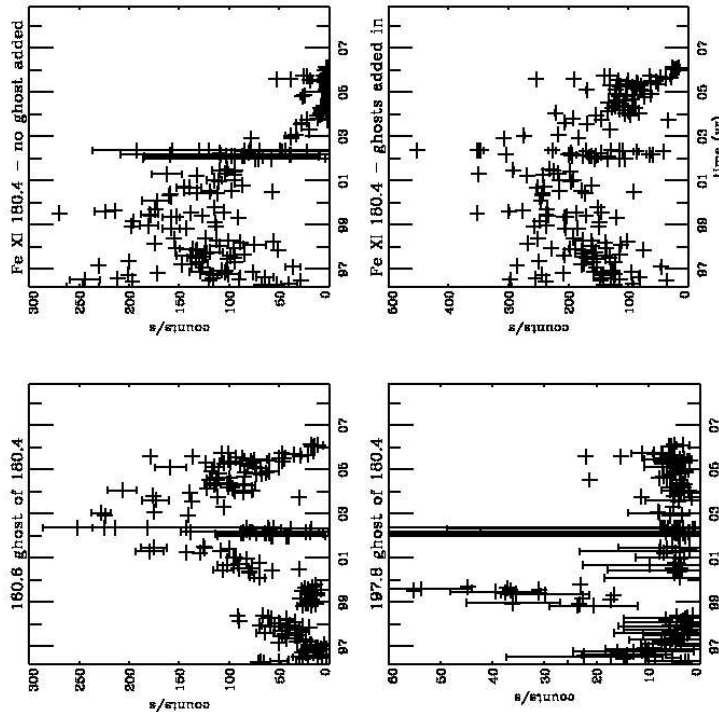


Figure 5. The count rates in the two ghosts (at 160.6 and 197.8 Å) of the Fe XI at 180.4 Å line (top panels), with the count rates in the Fe XI line (bottom panels). The changes in ghosting are an indication of changes in detector LUT parameters needed. For clarity, error bars are shown only for every fifth point.

the raw count rate history above the long term trends, which is found to be partly due to changes in ghosting for the lines affected, and partly due to sensitivity changes. Counts from ghosts can be relocated in the spectrum for lines that ghost into regions devoid of strong spectral lines. Table 3 lists these lines.

A good example is given in Figure 5 for Fe XI 180.4 Å which usually ghosts into the outer arm (showing at wavelength 160.6 Å) but at one period ghosted to the inner arm (at λ 197.8 Å). In the period 1996–1998 an increasing number of counts were lost to the outer arm, which is at the shorter wavelengths. After the SOHO loss of contact in 1998, there was a clear decrease in the ghosting at the shorter wavelength, and the appearance of a ghost at the longer wavelength (197.8 Å). This is the clearest evidence that the detector electronics gains had changed due to the SOHO attitude loss. The new gset of 1999 corrected this and the ghost at λ 197.8 Å disappeared, while the ghost at λ 160.6 Å became stronger. After 2005, the overall counts declined, which is partly due to LTGD and partly due to loss of counts from the ghost to the spectral arm further out.

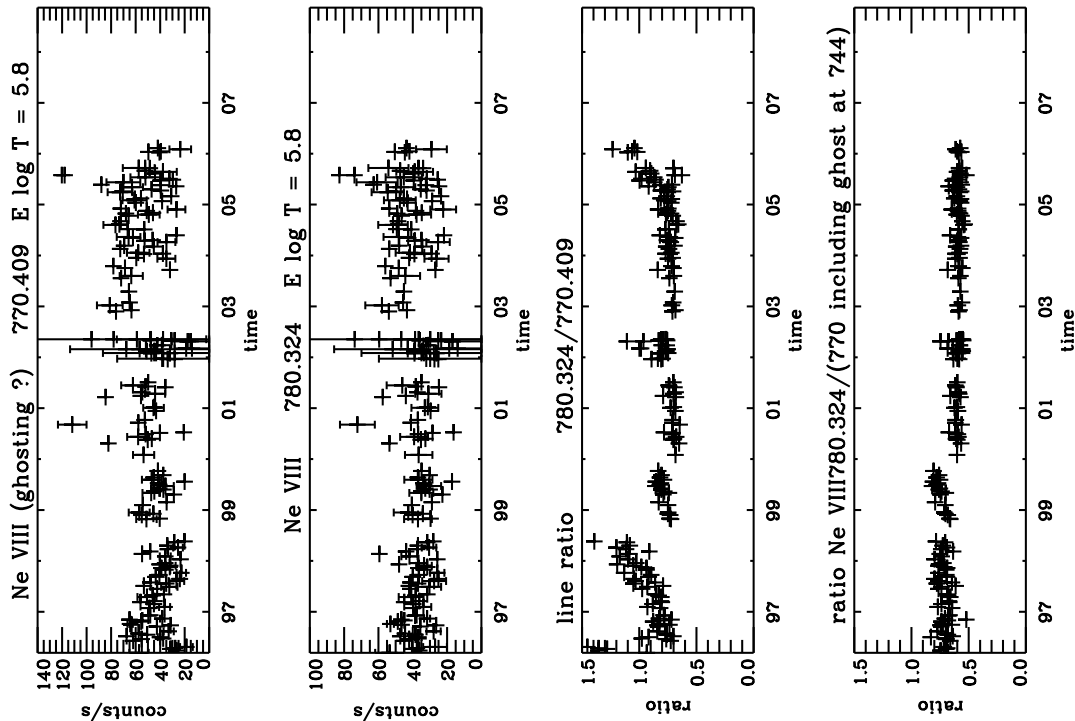


Figure 6. The count rates of the Ne VIII 780.3 Å and Ne VIII 770.4 Å doublet, together with their ratios, without and with the addition of the ghost to the 770.4 Å line. The line ratio clearly shows the variability in the ghosting. Once the ghost intensity is recovered, the line ratio becomes almost constant. The small discontinuity in 1999 can be attributed to the gset that was in use at the time. Error bars are shown for every fifth point.

In Figure 6 we see in the line ratio of the Ne VIII 770.4 Å and Ne VIII 780.3 Å lines evidence of changes in ghosting: we see that this happened in 1997, and again in 2005. The bottom panel of Figure 6 shows the raw count line ratio when the ghosted counts have been added back into the 770.4 Å line .

5.2. LINE WIDTHS

GIS line profiles are dominated by instrumental broadening. The line widths of strong lines show a clear increase over time, from 0.45 to 0.95 Å (cf. Figure 7). Notice that the same increases are found in all four detectors. These widths are derived from gaussian fits. Gaussian fits are not completely appropriate for some of the lines, due to the line shape distortion from the LTGD at line centre. However, they give a good indication of the variations in line widths.

Table 3. Ghosting GIS spectral lines which can be recombined with unblended ghosts

<i>line</i> λ (\AA)	ghosts λ 's	Emitting ions	Log T
174.5	154.6	Fe X	6.0
177.2	157.4	Fe X	6.0
180.4	160.6 & 197.8	Fe XI	6.1
182.2	162.8	Fe XI (bl Fe X)	6.1
184.5	165.4	Fe X (bl Fe XI)	6.0
185.2	166.2	Fe VIII	5.8
315.4	294.7 & 332.1	Mg VIII	5.9
335.3	318.6	Fe XVI (bl Mg VIII Fe XII)	6.3
436.7	408.7	Mg VIII (2)	5.9
770.4	744.2	Ne VIII	5.8

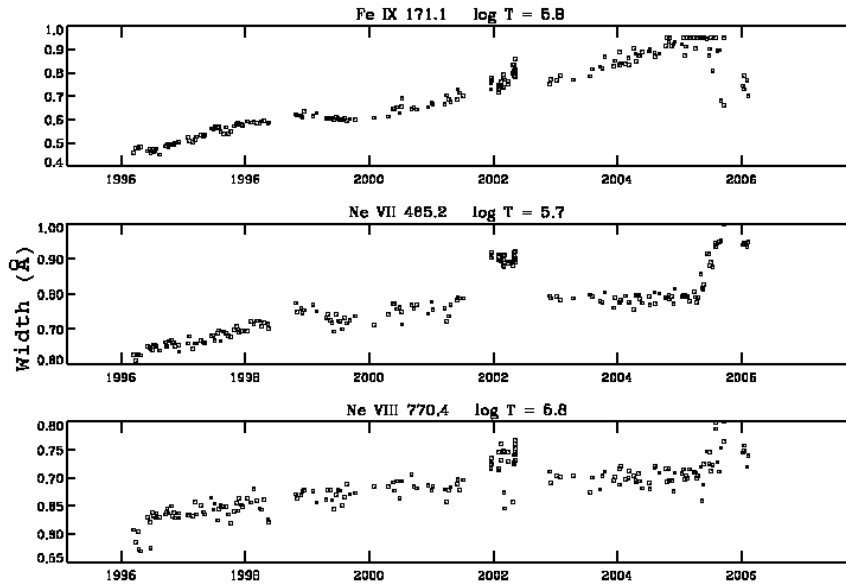


Figure 7. Line widths (in \AA) over time for three strong lines in detectors 1 (Fe IX), 3 (Ne VII), and 4 (Ne VIII).

The weaker lines, sometimes do not show much broadening over time at all, but show a larger spread in line widths than stronger lines. This may be due to low count rates.

Quite noticeable in Figure 7 are the G2AL observations, which tend to have broader lines. The 2005 data also show a large spread in the line widths

and large values of line widths, which we attribute to uncorrected gain loss, causing a supersensitivity in the detector response.

A possible explanation for the increase in line widths is that the MCP has many so-called channels per spectral line. Gain loss in the most exposed channels may have led the surrounding channels to become active. Cross-channel pulse propagation is perhaps made possible through enhanced induction effects within the MCP and may be related to the cause of the gain depression.

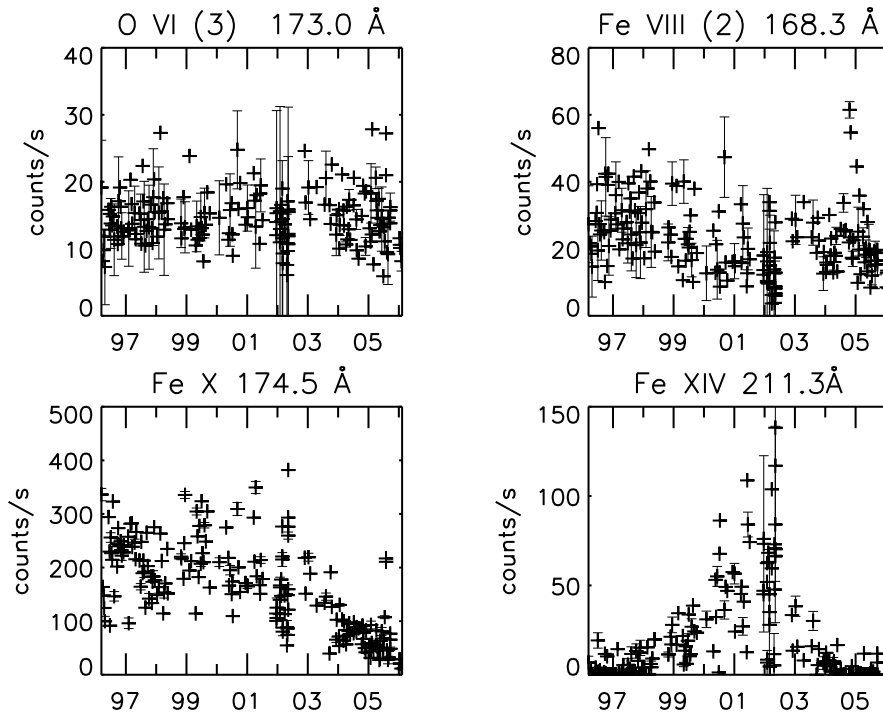


Figure 8. The raw count rates over time for some detector 1 lines. Notice the solar cycle effect in the hotter Fe XIV line. Error bars are shown only in each fifth point.

5.3. DETECTOR 1

The count rates for a selection of lines are shown in Figure 8. Detector 1 covers a spectral range where the strongest EUV coronal lines are. Most are formed at temperatures above 1 MK, hence clearly show the solar cycle variation. Parts of the detector show strongly ghosting lines, but most of this can be recovered. The strongest lines have suffered not only from ghosting but also from a reduction in sensitivity. The few weaker and cooler lines (O VI, Fe VIII) do not show significant variations over the cycle, which indicates that overall the instrument responsivity was stable.

Notice that the Fe XIV line shows a marked increase during solar maximum which peaked in 2001. To a lesser extent that increase is found also in the lower ionisation stages of Fe until it is too weak to measure in Fe X.

Early in 2005 the counts in detector 1 started falling and ghosts from lines like Fe XI 180.4 Å became very large compared to the primary line. The explanation is that operational detector voltages at that time were too low for good operation of detector 1 and counts were lost, as well as misplaced. The largest impact was in the lines that had LTGD. In May 2006 new gsets were implemented.

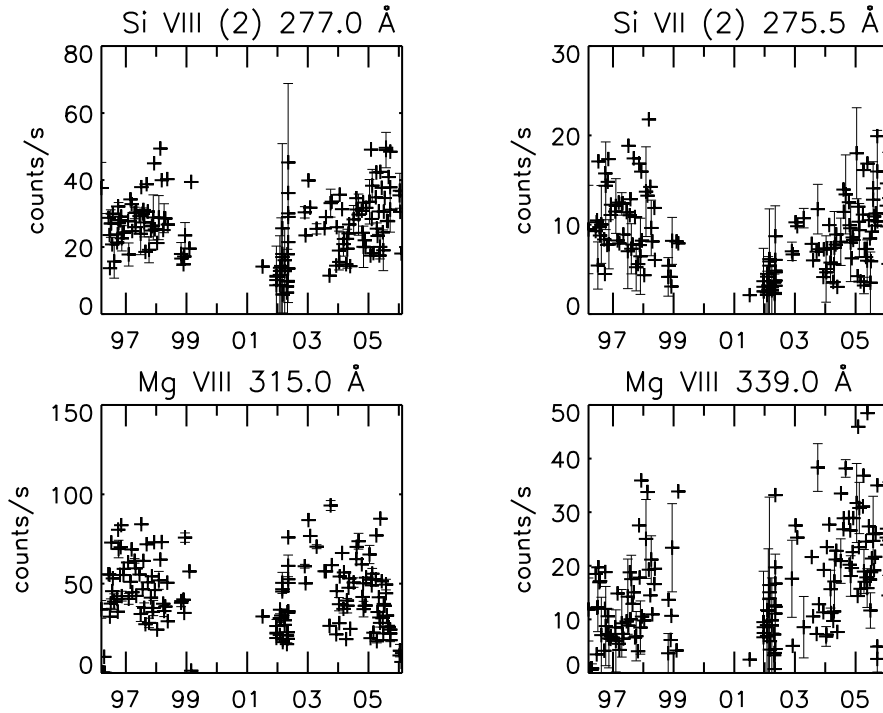


Figure 9. The raw count rates over time for some detector 2 lines. Error bars are shown every fifth point.

5.4. DETECTOR 2

Due to the presence of the He II 304 Å line, which has a very high count rate that tends to saturate the electronics, gsets were designed to have a low HV, essentially kept constant over time. In this way, the detector has been set to measure the weak lines. The sensitivity in the lines was nearly constant over time (see Figure 9), but strong ghosting is present in several lines. Changes in ghosting over time have also been identified in some lines.

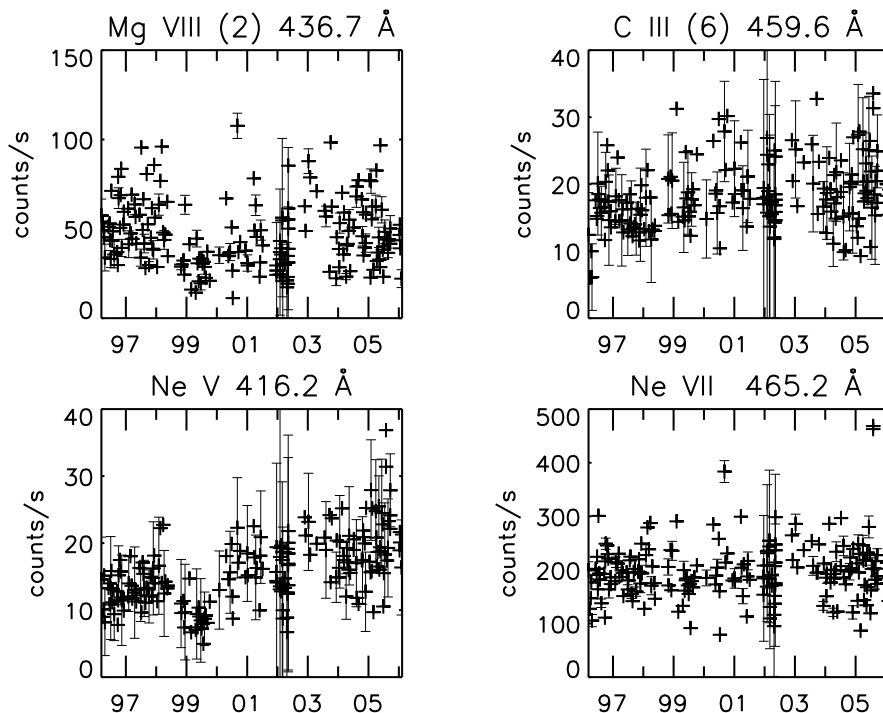


Figure 10. The raw count rates over time for some detector 3 lines. Error bars are shown every fifth point.

5.5. DETECTOR 3

Detector 3 contains a good selection of TR lines, with a few coronal lines (some in second order). This detector is virtually ghost-free. Remarkably, the raw counts of some TR lines have slightly increased over time (Figure 10). This can be explained by a higher efficiency of the MCP to produce good event PHDs so that fewer events are lost. Notice that in the period 1996–1998 the counts in nearly all lines tend to increase, while from mid-1998 to October 1999 the count rate seems anomalously low, or (sometimes) anomalously high. By considering the spectral lines on neighbouring spirals, for most lines this has been found to be due to changes in sensitivity, not to ghosting.

5.6. DETECTOR 4

Detector 4 contains a good selection of TR and coronal lines (in second order). Ghosting is present in some areas, but it is largely recoverable. In detector 4 all TR lines are either constant or show a slight increase in the raw count rates; see Figure 11. As in detector 3, there are drifts in the raw

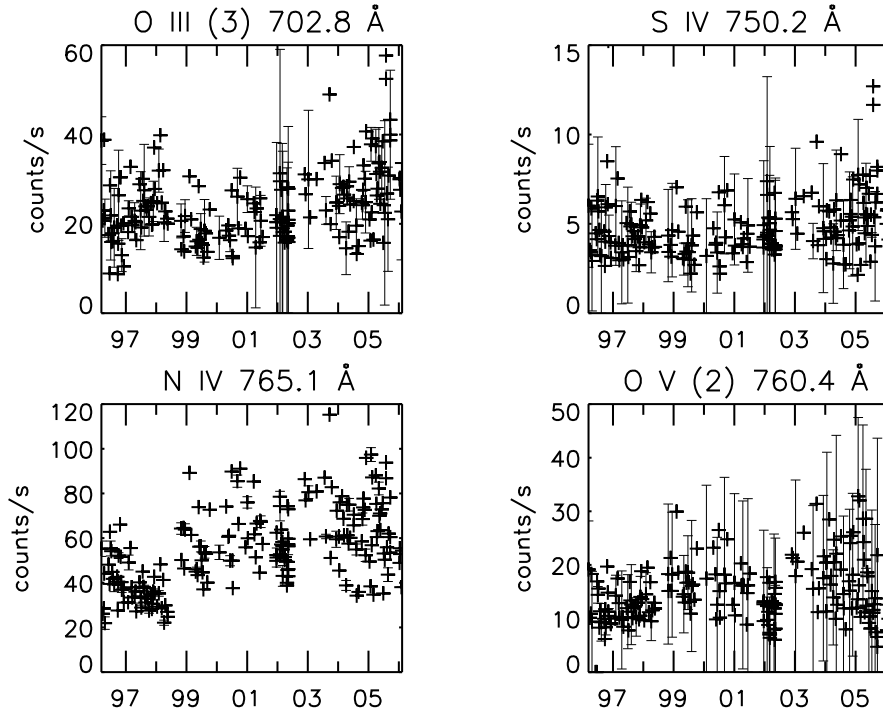


Figure 11. The raw count rates over time for some detector 4 lines. Error bars are shown every fifth point.

count rates in the period 1996–1998, which are partially, or wholly due to sensitivity changes. Notice that although the S IV line could be suspected to ghost, the raw counts show no evidence of any changes.

5.7. SENSITIVITY CHANGES

The simple count rate history already gives an indication of any major changes in the detectors. Lines formed at temperatures below 1MK do not show any significant changes, while the hotter ones clearly show solar-cycle effects. The weaker ones, however, have now (2006) returned to count rates similar to those measured in 1996. We have examined all the spectral lines by an automatic fit to their count rates, as a superposition of a linear behaviour with a gaussian (to model the increase during solar maximum), to identify the lines that were most affected by sensitivity changes, including LTGD. These lines are shown in Table 4. Note that some lines showed a considerable increase in sensitivity.

In the period that started with the SOHO loss of contact until the installation of new gsets in late 1999, there is a loss of sensitivity evident in

Table 4. Lines showing the largest change in count rate over time.

ION	Det.	λ	a_0	a_1	a_1/a_0
Fe XII	1	195.1	40	-1.12e-2	-2.83e-4
Fe IX	1	171.1	291	-6.58e-2	-2.26e-4
Fe X	1	174.5	236	-5.06e-2	-2.15e-4
Fe X	1	177.2	98	-2.12e-2	-2.17e-4
Fe XI	1	180.4	155	-3.00e-2	-1.94e-4
Fe XI	1	188.2	117	-2.10e-2	-1.79e-4
Fe XII	1	193.5	35	-5.57e-3	-1.60e-4
Fe X	1	184.5	61	-4.00e-3	-6.60e-5
Ne VIII	4	770.4	49	6.03e-3	1.23e-4
Ne V	3	416.2	12.4	2.16e-3	1.28e-4
Ne VII	3	465.2	188	5.09e-3	2.70e-5

Note: Included are the daily rates a_1 with an absolute value larger than 4.0×10^{-3} , where a_1 is defined by the linear relation:
raw counts = $a_0 + a_1 \times \Delta$ days.

a_0 is the raw count rate at on 12 March 1996.

In addition, some lines are included which have absolute rates of change relative to the initial count rate that are larger than 1.0×10^{-4} (more than 36% change over 10 years). Uncertainties in a_1 values are smaller than 20% (but smaller than 50% for Fe XII due to variability over the solar cycle.)

many lines, particularly in detectors 3 and 4. We attribute this to a change in the electronics performance, not a change in the MCPs.

Obviously, the dominant effect in the large scatter of values seen in the count rates is due to solar variability. The best way to remove it is to look at ratios of lines of the same ion or of ions that form at similar temperatures. We expect that LTGD effects would be mostly visible in the stronger lines, whilst the weaker ones would be less affected. Indeed this is what we have found. For most lines in each detector it is possible to find one or more suitable ratios. The few lines in detector 4 due to O III and N III show constant ratios. All the TR lines in detector 3 also show constant ratios. The few usable lines in detector 2 are weak but do not show any significant changes in their ratios. The ratios of lines in detector 1, on the other hand, clearly show LTGD. The strongest line is the Fe IX 171.1 Å. This line is not affected by ghosting and is therefore a good case to study LTGD. No other Fe IX lines are recorded by the GIS, but the Mg IX 368.1 Å is a weak second order line seen in detector 4, formed at a similar temperature. Figure 12 shows

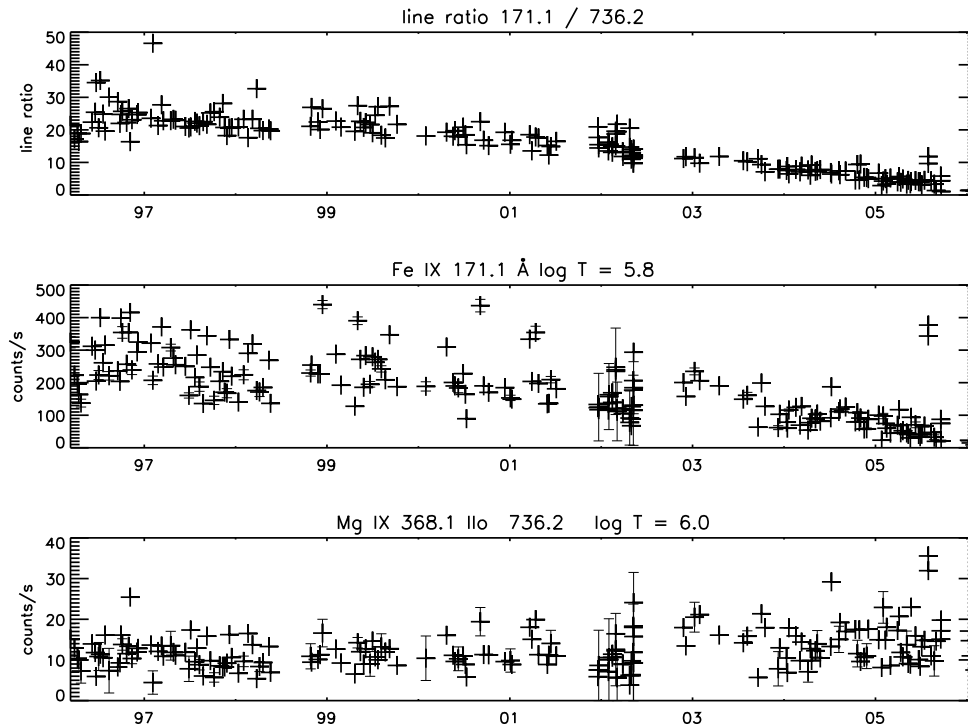


Figure 12. The line ratio of the total count rates of the Fe IX 171.1 Å and Mg IX 368.1 Å lines is shown in the top panel. The middle and bottom panel display the count rates of the two lines. The 171.1 Å line shows the strongest long term gain depression in the GIS. Error bars are shown for every fifth point.

the count rates for these two lines, together with their ratio, which clearly removes the solar variability and shows a steady LTGD after 2000.

After Fe IX 171.1 Å, the strongest lines in GIS 1 are due to Fe X. The 177.2 Å line shows clear ghosting from the Fe XII 195.1 Å line, on top of LTGD effects. The 174.5 Å line is affected by ghosting, but is recoverable. Its ratio with the much weaker 190.0 Å line (see Figure 13) also indicates significant LTGD.

After Fe X, the strongest lines are due to Fe XI. Significant LTGD were found only in the stronger 180.4 Å line after 2002, as evident from the ratio with the weaker 182.2 Å line (cf. Figure 14). The 188.2 Å line only shows small effects after 2003.

All data show problems of some degree in the 2005 period. In detector 1 the problem was worst because the HV setting was much too low by 2005, resulting in loss of sensitivity, evident in the the steeper declines in counts in 2005 in the $\lambda 171.1$ Å and $\lambda 180.4$ Å lines. From the drop in count rates in 2005 it is evident that detector 4 needed a new gset also. It is interesting to note that during the 2006 GIS 'tune-up' the drift in performance of detectors

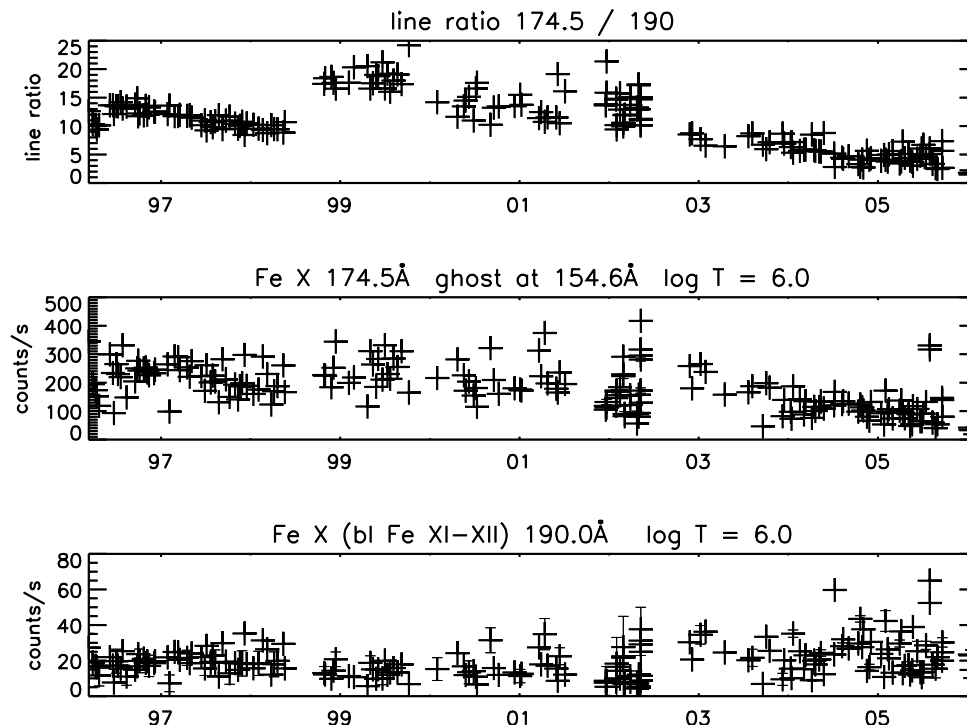


Figure 13. Ratio (top) with the count rates of the Fe x 174.5 (middle) and 190.0 Å (bottom) lines. The 174.5 Å stronger line has been corrected for ghosting. Error bars are shown for every fifth point.

2,3, and 4 turned out to be due to gain changes in the electronics, not the HV setting. We can also say with confidence that the ghosting from $\lambda 770.4$ Å (into $\lambda 744.2$ Å) in the quiet sun has been limited and can be clearly characterised.

6. Discussion and Conclusion

Our main aim was to investigate the GIS performance and to derive corrections to the sensitivity due to long term trends and other effects. We have concentrated on the quiet sun observations of 1996-2006 which provides a homogeneous data set over the solar cycle. In general, most lines have been remarkably constant over time, and only a few have shown clear trends in LTGD. The spectra have not degraded in time, with the exception of an overall steady increase in the line widths. Our analysis shows that the grazing-incidence optics and the detectors have performed exceptionally well, beyond any expectation.

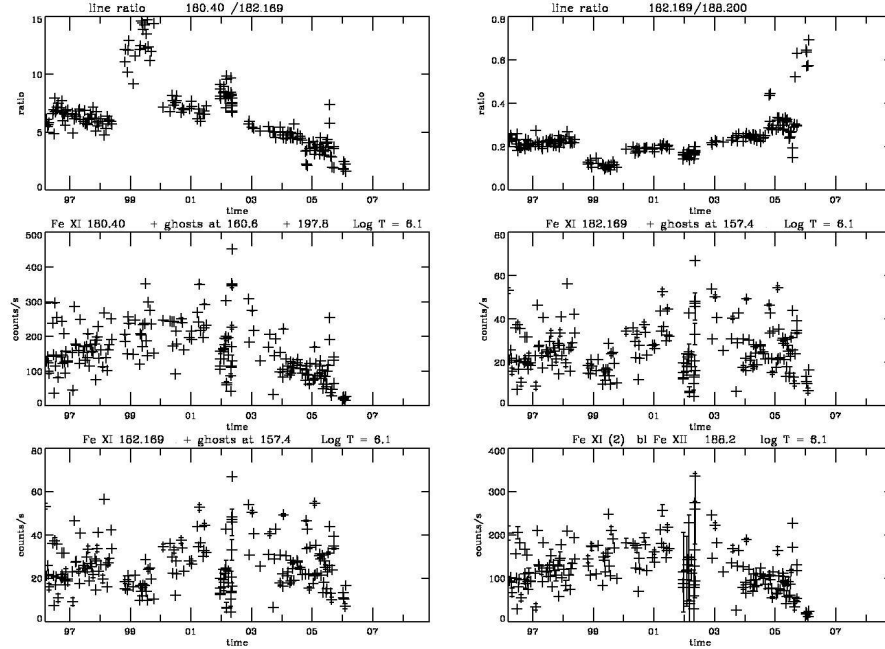


Figure 14. Line ratios with the count rates in Fe XI lines seen in detector 1. The strongest Fe XI 180.4 Å line shows significant LTGD after 2002 (the left three graphs show line ratio in the top panel and the count rate in each line in the middle and lower panel), while the weaker 188.2 Å is displayed in similar fashion in the right three graphs. The 188.2 Å line ratio shows small effects only after 2003. Error bars are shown for every fifth point.

Obviously, short-term sensitivity changes, in particular in active region observations, can be present in the data, if the count rates are high. For some periods sensitivity changes that diverged from the long-term trend have been observed which were probably due to changes in the detector and/or electronics and which were corrected at some point by installing new detector parameters (gsets).

For the lines with well-defined unblended ghosts, the total counts are consistent with the long-term gain depression trend. Anomalies fall into two broad categories, namely ghosting and sensitivity changes. The value of our approach has been that we can determine if a change in counts in one spiral arm is matched by an opposite change in neighbouring arms. If counts do not all show up in the next spiral arm, we conclude that there was (also) a change in sensitivity. We found further that using line ratios for lines of the same ion or similar ionisation temperature is useful as a diagnostic of problems. Several periods with anomalies stand out in these data, and corrections to long term trends are needed for these periods. The short term changes are related to the specific gsets: each time the gset is updated there is a return to the long-term trend.

We include a list of GIS lines that are considered reliable, without problems of ghosting, in the Appendix.

The decrease in sensitivity from line to line shows a large spread, and we are reluctant to say that the sensitivity trends can be generalised for all lines. We rather think that the sensitivity trends derived for each line, but consistent with line ratios of similar lines, should be used to derive the long-term response.

The fact that the raw counts have changed so little over time means that the calibration of Del Zanna et al. (2001), which was mainly based on mid-1997 data, is reliable. Some minor adjustments, mainly due to improvements in the atomic data, would be necessary. Our results give confidence in the use of GIS data for scientific use. We encourage the community to use the instrument in its best, high-cadence observations of strong TR and coronal lines.

The results reported in this paper provide the basis for a better calibration, which will be made available via solarsoft.

Acknowledgements

Support from PPARC is acknowledged.

Over the years, a large number of people have contributed to the operations and monitoring of the GIS instrument. These include members of the CDS team at GSFC, at RAL and MSSL. Particular efforts were provided by Eddie Breeveld, Barbara Bromage, Matthew Whyndham, John Lappington, Carl Foley, and Lucie Green.

NPMK would like to thank Alice Breeveld, Alan McCalden, Matthew Whyndham, and Lucie Green for helpful discussions, Ron Yurow for getting data, and Sarah Matthews for the opportunity to do this work. We thank an anonymous referee and Ken Philips for their detailed comments.

References

- Breeveld, A.A.: 1996, *Ph.D Thesis*, Univ. College London.
- Breeveld, A.A. and Thomas, P.D.: 1992, Proc. ESA Symp. on Photon Detectors for Space Instrumentation, *ESA-SP*, **356**, 237.,
- Brekke, P., Thompson, W.T., Woods, T.N. and Eparvier, F.G.: 2000, *Astrophys.J* **536**, 959.
- Bromage, B.J.I., Breeveld, A.A., Kent, B.J., Pike, C.D. and Harrison, R.A.: 1996, *Report of the Pre-Launch Calibration of CDS*, Univ. Central Lancashire, UCLan Report **CFA/96/09**.
- Del Zanna, G.: 1999, *Ph.D Thesis*, Univ. Central Lancashire.
- Del Zanna, G., Bromage, B.J.I., Landi, E., and Landini, M.: 2001, *Astron. Astrophys.* **379**, 708.

- Del Zanna, G., Andretta, V. and Beaussier, A.: 2005, *Mem. Sait.* **76**, 953.
- Del Zanna, G. and Andretta, V.: 2006, *ESA-SP*, **617**.
- Dere, K.P., Landi, E., Mason, H.E., Monsignori-Fossi, B.C., Young, P.R.: 1997, *Astron. Astrophys. Suppl. Ser.* **125**, 149.
- Harrison, R.A., Sawyer, E.C., Carter, M.K., Cruise, A.M., Cutler, R.M., *et al.*: 1995, *Solar Phys.* **162**, 233.
- Kuin, N.P.M. and Del Zanna, G.: 2006, *CDS Software Note* **57**.
- Landi, E., Del Zanna, G., Breeveld, E.R., Landini, M., Bromage, B.J.I., and Pike, C.D.: 1999, *Astron. Astrophys. Suppl. Ser.* **135**, 171.
- Lang, J., Kent, B.J., Breeveld, A.A., Breeveld, E.R., Bromage, B.J.I., Hollandt, J., Payne, J., Pike, C.D. and Thompson, W.T.: 2000, *J. Opt. A: Pure Appl. Opt.* **2**, 88.
- Lang, J., Thompson, W.T., Pike, C.D., Kent, B.J., and Foley, C.R.: 2002, in A. Pauluhn, M.C.E. Huber and R. von Steiger (eds.), *The Radiometric Calibration of SOHO*, ISSI Scientific Report **SR-002**, ESA Publications Division, Noordwijk, The Netherlands, 105.
- Lapington, J.S.: 2004, *private communication*.
- Malina, R.F. and Coburn, K.: 1984, *IEEE Transactions on Nuclear Science* **NS-31**, p. 404.
- Pauluhn, A., M.C.E. Huber, M.C.E. and von Steiger, R. (eds.), *The Radiometric Calibration of SOHO*, ISSI, Scientific Report **SR-002**, ESA Publications Division, Noordwijk, The Netherlands.
- Pauluhn, A. and Solanki, S.K.: 2003, *Astron. Astroph.* **407**, 359.
- Thompson, W.T.: 2006, *ESA-SP*, **617**, 80.

Appendix

A. Appendix

A.1. THE BEST GIS LINES

The lines in Table 5 were selected based on a combination of factors, including their location on the detector and the count rate history.

A.2. MATHEMATICAL DESCRIPTION OF ANODE AND EVENT PROCESSING

The theoretical model underlying the way that the data maps into a spiral has not been published in the generally available literature. In this section the basic derivation is outlined.

The insulating lines, drawn by laser, that divide the A , B , and C electrodes take the form of damped sine waves. To describe them, we define the X-coordinate along the spectral dispersion direction and have the electrodes interleave in a pattern A, B, C, A, B, C, A , etc. along the Y-axis. Each set of A , B , and C has a fixed height H_p , called the pitch height, and is identical in form. The electrodes of each kind (A, B , or C) are wire-bonded together. There is thus no positional information along the Y-axis.

The equations governing the height derive from the laser-etched lines dividing the electrodes.

Table 5. Prominent GIS spectral lines without ghost signature in their count rate history

λ (\AA)	ID's	Log T [K]
168.3	Fe VIII (2)	5.8
171.1	Fe IX	5.8
173.0	O VI (3)	5.5
186.9	Fe XII (2) (bl Fe VIII, Si XI)	6.2
188.2	Fe XI (2) (bl Fe XII)	6.1
190.0	Fe X (bl Fe XI-XII)	6.0
202.0	Fe XIII	6.2
202.7	Fe XI (bl O IV, S VIII)	6.1
203.2	Fe XII	6.2
275.5	Si VII (2)	5.8
277.0	Si VIII (2) (bl Mg VII, Si VII)	5.9
416.2	Ne V	5.5
417.3	Fe XV	6.3
444.0	Mg IX (bl Fe XIV)	6.0
448.3	Mg IX	6.0
465.2	Ne VII	5.7
466.2	Ca IX	6.0
748.4	S IV	5.1
749.6	Mg IX	6.0
750.2	S IV	5.1
760.4	O V (2)	5.4
780.3	Ne VIII	5.8

Notes: Numbers in parenthesis indicate self-blends;
 bl indicates a blend with lines from other ions;
 Ilo indicates a line in second order;
 Log T is the temperature of maximum ion abundance.

The bottom line is constant in Y, and for each time the pattern repeats the position shifts, and is given by:

$$y_1(n) = nH_p, \quad (1)$$

while

$$y_2 = y_1(n) + H_p/3 + a(x)\sin(\xi - \pi/3), \quad (2)$$

$$y_3 = y_1(n) + 2H_p/3 + a(x)\sin(\xi + \pi/3). \quad (3)$$

Note that the upper limit of the top electrode is $y_1(n+1)$, giving the total height of each set being H_p and the angle ξ ranges from 0 to 10π .

The width of electrodes is

$$w(A) = y_2 - y_1(n), \quad (4)$$

$$w(B) = y_3 - y_2, \quad (5)$$

$$w(C) = y_1(n+1) - y_3 = H + y_1(n) - y_3. \quad (6)$$

The amplitude a varies linearly along the dispersion direction.

$$a(x) = a(0) + \alpha\xi. \quad (7)$$

The extrema in the width are

$$w(B) = H_p/3 + \sqrt{3}a(x). \quad (8)$$

The number of cycles on the electrodes was set to be 5 in the X-direction. Let the total length of the electrode be L , then we can define

$$\xi = 5(2\pi)(x/L) \text{ radians}. \quad (9)$$

The minimum amplitude $a(0)$ was determined to be $45\mu\text{m}$ and the maximum amplitude $85\mu\text{m}$, so $\alpha=(85-45)/10\pi \mu\text{m} / \text{rad}$. The maximum width of the electrodes is thus $(390/3)+85 = 215 = (5/9) \times 390\mu\text{m}$. This factor is the maximum contribution from a flat signal to one electrode, and is used in the normalization of the signals in order to use the full digital range.

For any event, the average charge detected on any of the electrodes must be positive and proportional to the width of the electrodes. For each count there are two independent variables.

Let an event at some wavelength occur on the detector. The resulting charge cloud will give measured charges that can be represented as $A(:)w(A)$, $B(:)w(B)$, $C(:)w(C)$. The normalised charges are defined as: $A' = A/\Sigma$, $B' = B/\Sigma$, $C' = C/\Sigma$, with $\Sigma = (5/9)(A + B + C)$. We are only interested in the mean position of the event along the detector, i.e., as a function of x (or ξ). The analysis by (Breeveld, 1996) deals with the data space in detail, and the reader is referred there for a full discussion. We continue with the transformations needed for data processing.

The instrument electronics will normalise the charges from the three electrodes, digitize them, and output the measurement for two electrodes, i.e., A and B . Since 8-bit digitization is used, the range is 0-255.

We can recover C' from A' and B' from $C' = 460 - A' - B'$. Now the following transformations convert the data to a spiral in a plane:

$$X = (C' - B')/\sqrt{(2)}, \quad (10)$$

$$Y = (2A' - B' - C')/\sqrt{(6)}, \quad (11)$$

redefining X and Y in polar coordinates will allow the mapping of a spiral over the data:

$$r = \sqrt{(X^2 + Y^2)}, \quad (12)$$

$$\theta = \arctan(y/x) = \arctan((2 - 3(A' + B'))/(\sqrt{3}(A' - B'))). \quad (13)$$

The general form of the spiral to fit the data is

$$r = k(\theta + \phi), \quad (14)$$

with k the spiral expansion parameter, ϕ a zero point offset, and $0 < \theta < \text{inf}$. With each new arm the angle θ has increased by 2π .

It can be checked that θ is approximately proportional to ξ and periodically lags behind to catch completely up with ξ for each multiple of π .

Not the whole area of the electrode is used, since only part of the MCP front face is illuminated by the slit. See (Lang et al., 2000) for details. Typically the illuminated part is 50x16mm, with the 50mm being along the dispersion direction. This explains that only 4.2 cycles are seen in the raw data. Note that the use of 5.2 cycles was necessitated only due to the ghosting problem, but does not map further wavelengths.

The mapping from spectrum to pixel is based on the spiral equation, in that 4.2 (or 5.2) cycles map to 2048 pixels, equally spaced in ϕ .

Minor wiggles in the spiral arms were observed during testing (Breeveld, 1996) to depend on the ADC electronics gains and offsets. As a result, in modelling the spirals some of the parameters used in the mathematical model can be changed, namely the gain on each electrode and the multiplication factor for the sum-signal. These parameters are part of the gset used to build the on-board lookup table. The details of implementation can be found in the Solarsoft routine `view_raw`.

The mathematical description of the electrodes has been shown to lead to the particular data representation in the GIS, and we have established how to relate features in the data to the hardware.

A.3. FITS TO THE COUNT RATE HISTORY, USING LINE RATIO'S FOR INTERNAL CONSISTENCY

The following table lists the fits to the long term trend in the count rate histories. A linear fit was made to the whole period, as

$$cr = a_0 + a_1 \times N \quad (15)$$

where N is the number of days since an arbitrary day, being 1996-03-12, and cr the count rate.

Some spectral lines show during solar maximum an enhancement of the number of counts that can be modelled by adding a gaussian to a linear fit. The gaussian tends to peak in the 2001-2002 period. Using the fit, two points near solar minimum in 1996 and 2006 are chosen to derive a long term trend in sensitivity for that line and has been entered in the table. The derived accuracy depends in the remaining raw count rate near the minimum and the derived trend is therefore not very reliable for averaged raw count rates less than 1.

For certain periods some lines deviate from the general trend, which may be due to sensitivity loss/gain, ghosting, or both. Sensitivity loss/gain may occur if the gset was not optimal for the solar conditions of the observation, or due to instrumental changes. We used two methods to separate out these contributions. Spectral lines that are formed at the same angles in the data spiral were plotted next to each other. In the case of ghosting, counts are relocated. In the case of sensitivity loss, relocating counts will not resolve the problem, and it must be due to sensitivity loss. We also used line ratios. In the case of equal sensitivity loss in two lines, the line ratio is constant, while when ghosting is present it is not. An exception would be if the ghosting were to stay constant in size, but that seems not to happen.

We have thus been able to derive the long term trends and periods of sensitivity loss for many lines. The tables below show the initial fits to the count rate histories.

Table 6. GIS 1 spectral lines count rate history fit

λ (\AA)	ID's & Log T	a_0	a_1
s=sens.ch.			
g=ghost	time range		
164.500	Ni XIII ?	7.95	-1.424e-03
168.300	Fe VIII log T = 5.8	27.61	-3.549e-03
171.072	171.072 Fe IX log T = 5.8	290.82	-6.584e-02
s	1996-03-12-1996-04-23:	312.77	-4.374e+00
s	2002-11-25-2003-10-03:	720.24	-2.102e-01
173.000	173.000 O VI (3) log T = 5.5	14.04	-3.0e-5
174.534	Fe X (bl O V) 174.5+ghost 154.6 log T = 6.0	235.7	-0.051
177.242	Fe X 177.2+ ghost 157.400 log T = 6.0	97.9	-0.021
180.40	Fe XI (bl Fe X) 180.4+ 160.6 log T = 6.1	154.7	-0.030
182.200	Fe XI (bl Fe X 182.2+162.800 log T = 6.1	24.00	0.00
184.0	Fe X (bl Fe XI) 184.0+165.4 log T = 6.0	60.27	-0.006
185.0	Fe VIII 185.0 + ghost 166.200 log T = 5.8	24.96	-1.864e-03
	2002-11-25-2005-05-23:	11.23	1.009e-02
	2005-06-09-2006-02-09:	570.37	-1.544e-01
186.880	Fe XII (2)) (bl Fe VIII) log T = 6.2	20.5	-0.0019
188.200	Fe XI (2) bl Fe XII log T = 6.1	117.1	-0.021
190.000	Fe X (bl Fe XI-XII) log T = 6.0	16.57	-1.0e-03
193.521	Fe XII (bl Fe XI cont 175.3 ?) log T = 6.2	34.9	-5.57e-03
195.100	Fe XII (3) (ghosting-cont 177.2 ?) log T = 6.2	39.6	-0.011
198.700	S VIII (bl)	4.43	-3.992e-04
	1998-10-27-1999-10-08:	0.19	5.380e-03
201.128	Fe XIII (ghosting 184 ?) log T = 6.2	9.06	-9.734e-04
202.044	Fe XIII (bl) (gh-cont 185.2) log T = 6.2	22.5	-3.29e-03
202.700	Fe XI (bl) log T = 6.1	9.29	-1.0e-04
	2001-12-18-2002-05-10:	14.28	-4.969e-03
203.200	Fe XII + Fe XIII (bl) log T = 6.2	0.63	-1.05e-04
	2004-11-26-2006-02-09:	12.98	-2.936e-03
203.800	Fe XIII (2) (gh-cont 186.88) log T = 6.2	6.13	0.0
211.320	Fe XIV (bl r-ghosting 196.5) log T = 6.2	4.65	-1.52e-03

Table 7. GIS 2 spectral lines count rate history fit

λ (\AA)	ID's & Log T	a_0	a_1
s=sens.ch.			
g=ghost	time range		
271.983	Si X (+ghosted 295.0) log T = 6.1	6.84	3.246e-03
272.638	Si VII (ghosted by 296.2) log T = 5.8	2.87	1.262e-03
275.500	Si VII (2) log T = 5.8	9.46	-3.081e-04
277.000	Si VIII (bl Mg VII Si VII) log T = 5.9	25.81	8.704e-04
	2001-12-18-2002-05-10:	-128.9	6.561e-02
278.400	Mg VII (bl Si VII) log T = 5.8	9.65	-8.309e-04
	2001-12-18-2002-05-10:	2.93	0.000e+00
280.000	O IV log T = 5.3	5.27	-9.261e-04
	2001-12-18-2002-05-10:	14.84	-6.123e-03
284.160	Fe XV bl Al IX (ghosting 306) log T = 6.3	10.0	0.00
290.690	Si IX bl Fe X-XII (r-ghosting 266.9 +ghost 311.4) log T = 6.0	8.74	-1.403e-04
	1996-03-12-1998-05-20:	5.06	1.128e-02
	1998-10-27-1999-02-26:	3.24	0.000e+00
	2001-12-18-2002-05-10:	-83.10	4.116e-02
292.800	Si IX (3) log T = 6.0	8.30	-7.593e-04
s	1996-03-12-1998-05-20:	5.97	1.836e-02
	1998-10-27-1999-02-26:	2.46	0.000e+00
	2001-12-18-2002-05-10:	-67.82	3.357e-02
294.000	Ar VI ? (ghost 314.3) log T = 0	2.71	-1.352e-04
	1996-03-12-1998-05-20:	1.09	4.794e-03
	1998-10-27-1999-02-26:	0.07	9.259e-04
	2001-12-18-2002-05-10:	-29.07	1.411e-02
	2002-11-25-2005-06-09:	4.09	-7.445e-04
	2005-06-09-2006-02-09:	-174.9	5.249e-02
296.117	Si IX (2) (r-ghosting 272.6) log T = 6.0	31.79	-1.010e-04
	1996-03-12-1998-05-20:	25.81	2.247e-02
311.796	Mg VIII (bl r-ghosting 290.7, b-ghosting 329.3) log T = 5.9	10.31	5.660e-04
313.754	Mg VIII log T = 5.9	23.92	1.030e-03
314.327	Si VIII (bl) (r-ghosting 294.1) log T = 5.9	11.56	-3.099e-04
315.038	Mg VIII (315.0 + ghost 294.7) log T = 5.9	56.18	-1.914e-03
316.205	Si VIII log T = 5.9	27.96	8.482e-06
317.038	Mg VIII (bl Fe) 317.0+ghost 296.8 log T = 5.9	17.93	-1.312e-03
319.825	Si VIII (ghosting 336.1 299.9) log T = 5.9	49.83	7.198e-04
320.809	Fe XIII (bbl ghosting-cont 337.2) log T = 6.2	5.07	2.848e-03
325.000	Al VIII (bl +ghost) log T = 6.3	0.44	-7.257e-05
332.789	Al X (bl Ca IV Fe X) log T = 6.0	9.53	2.325e-03
334.172	Fe XIV log T = 6.2	0.766	-2.8e-04
335.3	Fe XVI bl Mg VIII Fe XII (335.3 + 318.6) log T = 6.3	18.13	-2.61e-03
336.1	ghost 319.8	3.55	5.269e-04
	1996-03-12-1998-05-20:	0.78	9.982e-03
	2001-12-18-2002-05-10:	-5.39	3.468e-03
337.257	Ar VIII ? (ghost-cont 320.8) log T = 5.6	3.55	2.923e-03
	1996-03-12-1998-05-20:	1.09	1.297e-02
	2001-12-18-2002-05-10:	-16.76	9.652e-03
338.278	Fe XII (bl Fe X) log T = 6.2	11.46	2.316e-04
	2001-12-18-2002-05-10:	-70.56	3.527e-02
339.006	Mg VIII (bl Ca VII) log T = 5.9	9.24	3.522e-03
	2001-12-18-2002-05-10:	-4.54	6.405e-03

Table 8. GIS 3 spectral lines count rate history fit

λ (\AA)	ID's & Log T	a_0	a_1
s=sens.ch.			
g=ghost	time range		
395.555	O III log T = 5.1	3.28	-6.074e-05
	1996-03-12-1998-05-20:	3.50	1.235e-03
	1998-10-27-1999-10-08:	1.92	-4.618e-04
	2000-01-31-2002-05-10:	6.69	-2.196e-03
	2002-11-25-2006-02-09:	6.49	-9.255e-04
399.821	Ne VI bl Fe XIII Ilo log T = 5.6	9.16	6.873e-04
s	1998-10-27-1999-10-08:	5.48	-4.993e-04
s	2001-12-18-2002-05-10:	-5.70	6.101e-03
400.666	Mg VI (bl Fe XIII Ilo +ghost ?) log T = 5.7	6.66	1.192e-04
401.136	Ne VI (bl) log T = 5.6	16.16	2.078e-03
	1998-10-27-1999-10-08:	19.42	-7.966e-03
401.926	Ne VI bl Fe XIII Ilo (+ghost 430.5) log T = 5.6	41.04	2.292e-03
s	1998-10-27-1999-10-08:	41.80	-1.104e-02
403.300	Mg VI + Ne VI log T = 5.7	22.06	2.095e-03
411.150	Na VIII (+ghost 439.2 ?) log T = 5.9	9.59	-1.484e-04
s	1998-10-27-1999-10-08:	6.02	-1.356e-03
s	2001-12-18-2002-05-10:	-10.86	7.419e-03
416.194	Ne V log T = 5.5	12.36	2.157e-03
s	1998-10-27-1999-10-08:	13.00	-3.788e-03
416.843	Ne V (bl) log T = 5.5	1.85	-4.025e-05
417.258	Fe XV (bl) log T = 6.3	1.52	1.361e-03
419.713	C IV (bl Ca X Fe XIII Ilo) log T = 5.1	13.45	1.535e-03
s	1998-10-27-1999-10-08:	8.46	1.568e-03
429.140	Mg VII log T = 5.8	3.82	3.830e-04
s	1998-10-27-1999-10-08:	4.56	-1.700e-03
s	2001-12-18-2002-05-10:	-7.68	5.151e-03
430.465	Mg VIII (bl O II ?) log T = 5.9	30.58	-2.237e-04
s	1998-10-27-2001-07-05:	6.88	1.067e-02
431.200	Mg VII (2) log T = 5.8	11.07	2.548e-04
s	1998-10-27-2001-07-05:	4.19	3.068e-03
434.700	Mg VII (3) (bl Fe XII 217.276 Ilo r-ghosting 406.8?) log T = 5.8	22.16	8.292e-04
	1998-10-27-1999-10-08:	15.04	-9.187e-04
435.648	Ne VI (bl Ca VIII r-ghosting 407.7 ? +ghost 459.6) log T = 5.6	10.46	1.023e-03
	1998-10-27-1999-10-08:	11.79	-3.253e-03
436	Mg VIII (2) (436.7+ghost 408.9) log T = 5.9	51.50	-6.125e-04
s	1998-10-27-1999-10-08:	33.74	-4.452e-03
436.700	Mg VIII (2) (r-ghosting 408.9) log T = 5.9	50.32	-1.445e-03
s	1998-10-27-1999-10-08:	33.76	-4.659e-03
439.176	Mg IX (bl r-ghosting 411.1) log T = 6.0	1.29	-2.862e-06
s	1998-10-27-1999-10-08:	-0.08	2.901e-04
441.199	Mg IX (bl Ca VIII) log T = 6.0	2.50	6.477e-04
	1998-10-27-2001-07-05:	0.65	1.614e-04
	2001-12-18-2002-05-10:	-7.68	5.151e-03
443.973	Mg IX (bl) log T = 6.0	10.04	9.991e-04
448.293	Mg IX log T = 6.0	2.99	-4.999e-05
	2001-12-18-2002-05-10:	-11.47	5.946e-03
	1998-10-27-1999-10-08: <code>gis_sensitivity.tex</code> ; 12/10/2007; 23:53:19:33	15.38	-3.017e-04
459.600	C III (3) (bl +ghost 480.4? ,ghosting/ed 435.6) log T = 5.0	15.38	1.271e-03
465.220	Ne VII log T = 5.7	188.45	5.089e-03
466.239	Ca IX (bl Fe XIII Ilo) log T = 5.8	19.63	1.783e-03
	1998-10-27-1999-10-08:	20.01	-4.352e-03
	2001-12-18-2002-05-10:	-13.18	1.420e-02

Table 9. GIS 4 spectral lines count rate history fit

λ (\AA)	ID's & Log T	a_0	a_1
s=sens.ch.			
g=ghost	time range		
685.000	N III (bl) log T = 5.0	1.81	2.800e-04
685.800	N III (bl) log T = 5.0	10.41	1.243e-03
702.332	702.332 O III (bl Mg V IIo) log T = 5.0	5.06	2.566e-04
	1996-03-12-1996-04-23:	3.42	-8.190e-03
	1996-06-06-1998-05-20:	13.02	-6.580e-03
702.800	O III (2) log T = 5.0	11.80	4.880e-03
703.850	O III (2) (bl Fe XII IIo) log T = 5.0	38.1	1.097e-4
704.200	Fe XII 352.13 IIo (bl O III) log T = 6.1	1.57	4.135e-04
s	1998-10-27-1999-10-08:	1.01	-1.576e-04
s	2000-01-31-2001-07-05:	-1.53	1.762e-03
704.800	Unid. 704.800	0.64	9.850e-05
705.300	Fe XI (bl) 352.662 IIo log T = 6.1	1.06	2.011e-04
s	1996-06-06-1998-05-20:	4.90	-9.376e-04
706.060	Mg IX (bl +ghosted by 737.9) log T = 6.0	1.19	1.020e-03
718.600	O II (4) (bl Ne V 359.4 IIo) (ghosting to 685.0) log T = 4.8	4.26	1.520e-03
g+s	1996-03-12-1998-05-20:	10.32	3.538e-03
728.900	S III bl Fe XII 364.467 IIo log T = 6.1	2.07	2.004e-04
s?	1996-03-12-1998-05-20:	3.88	1.141e-03
735.300	Mg VII (2) 367.67 IIo log T = 5.8	1.00	1.403e-04
	1996-03-12-1998-05-20:	0.45	-4.058e-04
736.140	Mg IX 368.070 IIo log T = 6.0	10.27	9.174e-04
738.200	Fe XI 369.1 IIo (ghosting to 706.5 + ghosted by 765.1) log T = 6.1	6.00	2.500e-03
g	1996-06-06-1998-05-20:	4.01	1.863e-02
s	2001-12-18-2002-05-10:	76.19	-2.328e-02
	2005-06-09-2006-02-09:	-48.05	2.344e-02
748.392	S IV log T = 5.1	2.13	9.082e-05
749.551	Mg IX (+ghost?) log T = 6.0	0.508	-1.100e-04
750.220	S IV log T = 5.1	4.07	3.130e-04
755.600	Ca IX 378.081 IIo log T = 5.8	1.13	-2.660e-04
s	1996-03-12-1998-05-20:	0.16	-1.520e-05
758.676	O V (bl Ne III IIo) log T = 5.4	0.76	1.20e-03
759.441	O V (bl O IV IIo) log T = 5.4	0.67	1.10e-03
760.400	O V (2) log T = 5.4	12.44	9.826e-04
762.003	O V log T = 5.4	0.94	1.38e-03
765.146	N IV (ghosting 738.2) log T = 5.2	53.89	2.967e-03
s	1996-06-06-1998-05-20:	48.15	-2.399e-02
g	1996-03-12-1996-04-23:	48.44	-5.589e-01
768	Unid. (768.7+ghost 7423)	5.91	6.858e-04
s	1998-10-27-1999-10-08:	3.60	0.000e+00
768.700	Unid.	4.16	7.242e-04
s+g	1998-10-27-1999-10-08:	5.32	-1.499e-03
770	Ne VIII (770.4+ghost 744.0) log T = 5.8	49.18	6.033e-03
770.409	Ne VIII log T = 5.8	38.97	4.148e-03
g	1996-03-12-1996-04-23:	51.29	-7.964e-01
g	1996-06-06-1998-05-20:	56.46	-3.274e-02
780.324	Ne VIII log T = 5.8	35.59	1.654e-03